

On the Dust Signatures Induced by Eccentric Super-Earths in Protoplanetary Disks

YA-PING LI(李亚平),¹ HUI LI(李晖),¹ SHENGTAI LI(李胜台),¹ AND DOUGLAS N. C. LIN(林潮)²

¹Theoretical Division, Los Alamos National Laboratory, Los Alamos, NM 87545, USA

²Department of Astronomy and Astrophysics, University of California, Santa Cruz, CA 95064, USA

ABSTRACT

We investigate the impact of a highly eccentric $10 M_{\oplus}$ (where M_{\oplus} is the Earth mass) planet embedded in a dusty protoplanetary disk on the dust dynamics and its observational implications. By carrying out high-resolution 2D gas and dust two-fluid hydrodynamical simulations, we find that the planet's orbit can be circularized at large radii. After the planet's orbit is circularized, partial gap opening and dust ring formation happen close to the planet's circularization radius, which can explain the observed gaps/rings at the outer region of disks. When the disk mass and viscosity become low, we find that an eccentric planet can even open gaps and produce dust rings close to the pericenter and apocenter radii before its circularization. This offers alternative scenarios for explaining the observed dust rings and gaps in protoplanetary disks. A lower disk viscosity is favored to produce brighter rings in observations. An eccentric planet can also potentially slow down the dust radial drift in the outer region of the disk when the disk viscosity is low ($\alpha \lesssim 2 \times 10^{-4}$) and the circularization is faster than the dust radial drift.

Keywords: accretion, accretion disks — protoplanetary disks — planets and satellites: rings — planetdisk interactions

1. INTRODUCTION

Strong observational evidence for the existence of multiple dust rings/gaps in disks has emerged from high-resolution observations with the Atacama Large Millimeter Array (ALMA), e.g., HL Tau (ALMA Partnership et al. 2015), TW Hya (Andrews et al. 2016; Tsukagoshi et al. 2016), HD 163296 (Isella et al. 2016), AA Tau (Loomis et al. 2017), Elias 24 (Cieza et al. 2017; Cox et al. 2017; Dipierro et al. 2018), AS 209 (Fedele et al. 2018), GY 91 (Sheehan & Eisner 2018), V1094 Sco (Ansdell et al. 2018; van Terwisga et al. 2018), MWC 758 (Boehler et al. 2018; Dong et al. 2018a), including several recent surveys of young disks (Long et al. 2018; Andrews et al. 2018; van der Marel et al. 2019). A large fraction of these rings are located at the outer region of the disks, i.e., $\sim 50 - 100$ au. Planet-disk interaction (e.g., Dipierro et al. 2015; Dong et al. 2015; Pinilla et al. 2015; Jin et al. 2016; Dong et al. 2017, 2018b) is one of the main mechanisms that are proposed to produce these rings, although several other scenarios have also been proposed (e.g., Pinilla et al. 2012; Takahashi, & Inutsuka 2014; Gonzalez et al. 2015; Suriano et al. 2017, 2018; Zhang et al. 2015; Okuzumi et al. 2016; Miranda et al. 2017). It is generally

thought that forming (sometimes massive) planets *in situ* at such large disk radii is quite difficult. It is then worthwhile to explore whether there are mechanisms that deliver planets to such large radii even though other may be born at relatively small disk radii.

Observationally, many exoplanets discovered so far are found to be in highly eccentric orbits¹. Planet-disk and/or planetary scattering may be responsible for the eccentricity for the inner “hot Jupiter” such as CI Tau (Duffell & Chiang 2015; Rosotti et al. 2017) while delivering other planets into the outer region of the disk by the eccentricity pumping, where three rings were discovered (Clarke et al. 2018). Multiple planet-planet scattering is a promising mechanism that delivers planets from a few au where they were likely born to the outer disk region by exciting the planet's orbit to a high eccentricity, which then circularizes at a large radius. In addition, many previous studies have examined the eccentricity excitation of massive gas giants (e.g., Rasio, & Ford 1996; Jurić & Tremaine 2008; Marzari et al. 2010; Moeckel & Armitage 2012; Lega et al. 2013; Rosotti et al. 2017). Furthermore, an eccentric orbit could also be the relics due to the planet-disk interaction (e.g., Papaloizou et al. 2001; Goldreich & Sari 2003; Bitsch et al. 2013; Duffell & Chiang 2015), secular chaos (Wu, & Lithwick 2011), Kozai-Lidov oscilla-

Corresponding author: Ya-Ping Li
leey2009@gmail.com

¹ <http://exoplanets.org/>

tions (Kozai 1962; Lidov 1962; Takeda, & Rasio 2005). In the planet-disk interaction scenario, whether the eccentricity can be excited or damped depends on the dominance of Lindblad and co-rotation resonance torque (Goldreich & Sari 2003; Duffell & Chiang 2015). It is found that a Jupiter mass planet can pump up its orbital eccentricity due to the interaction with the disk (D’Angelo et al. 2006).

In this study, we investigate the impact of a highly eccentric super-Earth on the dust distribution during its orbital evolution. (The effect of an eccentric massive giant will be studied in a future work.) Our main goal of this paper is to explore whether an eccentric super-Earth can leave observational features in a dusty disk, and how these features can be used to infer the planetary properties. Previous studies on eccentric planets mainly focused on the planet migration and circularization timescales, which have either used the linear theory when the eccentricity is small (e.g., Goldreich & Tremaine 1978, 1980; Papaloizou & Larwood 2000; Papaloizou et al. 2001; Tanaka & Ward 2004; Duffell & Chiang 2015), or the non-linear simulations with an initially large eccentricity (e.g., Cresswell et al. 2007; Bitsch et al. 2013), but the influence on dust has not been explored self-consistently.

The paper is organized as follows. The numerical simulation setup will be described in Section 2. We present the results in Section 3, and discussions and conclusions are given in Section 4.

2. METHOD

We use the LA-COMPASS code (Li et al. 2005, 2009; Fu et al. 2014) to simulate the coupled gas-dust and planet dynamics. The main ingredient of our model is that one planet with a mass of $M_p = 10 M_\oplus$ in an eccentric orbit, where M_\oplus is the Earth mass, is embedded in the dusty disk. The planet orbits around the star with an initial orbital eccentricity e_p and a semi-major axis of a_p . The planet is initially located at the pericenter of the orbit. After 10 orbital evolution with a fixed orbit, the planet is freely released by considering the dynamical interaction between the disk and the planet. For all models listed in Table 1, we adopt a softening length of $0.7h_g$ for the planet’s potential, where h_g is the disk gas scale height. These runs are used to understand the dependence of orbital evolution of eccentric planets on disk gas surface density, initial orbital eccentricity, disk viscosity, dust particle sizes, and their consequent influence on the dust dynamics as well.

A disk, extending from 10 to 500 AU, around a pre-main sequence (PMS) star with a mass of $M_\star = 1.0 M_\odot$ is considered. The disk gas surface density is initially described by

$$\Sigma_g(r) = \Sigma_0 \left(\frac{r}{r_c}\right)^{-\gamma} \exp\left[-\left(\frac{r}{r_c}\right)^{2-\gamma}\right], \quad (1)$$

where $r_c = 150$ au and $\gamma = 1.0$. The normalization of gas surface density Σ_0 is treated as one main free parameter to determine the total disk mass. We have considered two disk masses with $M_{\text{disk}} = 0.02 M_\odot$ and $5 \times 10^{-3} M_\odot$, or equivalently $\Sigma_0 = 1.4 \text{ g cm}^{-2}$ and 0.36 g cm^{-2} , respectively. Disk self-gravity is considered for all models (Li et al. 2009) since the minimum Toomre Q parameter can reach ~ 2 after the planet is circularized.

We choose a locally isothermal equation of state (EoS) with the sound speed c_s given by

$$\frac{c_s}{v_K} = \frac{h_g}{r} = h_0 \left(\frac{r}{r_0}\right)^{0.25}, \quad (2)$$

where $r_0 = 50$ au. And $h_0 = 0.03$ is adopted as a typical value for the sound speed. v_K is the Keplerian velocity. Note that Equation (2) also expresses the radial profile of the gas scale height h_g/r . The effect for a different adiabatic EoS is discussed in detail in Appendix A. The disk viscosity is adopted from the Shakura-Sunyaev prescription $\nu_g = \alpha_{\text{vis}} c_s h_g$ with a constant α_{vis} across the whole disk (Shakura & Sunyaev 1973). A single dust species with its size s_d as listed in Table 1 is included in the simulations. We assume that the initial dust surface density Σ_d follows the gas profile Σ_g , with an initial dust-to-gas ratio of 1%. In the Epstein regime for the disk and dust parameters of interest here, the Stokes number of the particles with dust radius s_d in the mid-plane of the disk is defined as

$$\text{St} = \frac{\pi \rho_s s_d}{2 \Sigma_g}, \quad (3)$$

where ρ_s is the solid density of the dust particle. $\text{St}(r_0) = 0.01$ for our fiducial model, which is the main parameter that controls the radial drift of dust.

We solve the hydrodynamics equations with a high-resolution 2D grid of $(n_r, n_\phi) = 3072 \times 3072$ in the radial and azimuthal direction. We have tested that an even higher resolution of $(n_r, n_\phi) = 6144 \times 6144$ does not change the results significantly. A fixed boundary condition is applied to the gas, while an outflow inner boundary condition and outer boundary condition are imposed on the dust, which allow the dust flow out/in from the boundary depending on its radial velocity.

In order to identify the observational features from the dust, we follow Li et al. (2019) to obtain the dust continuum emission at mm wavelengths using the RADMC-3D package (Dullemond et al. 2012). To convert the 2D dust surface density produced from hydrodynamical simulation into a 3D grid, we adopt a dust scale height $h_d = h_g \min\left(1, \sqrt{\frac{\alpha_{\text{vis}}}{\min(0.5, \text{St})(1 + \text{St}^2)}}\right)$ by considering the dust vertical settling (Birnstiel et al. 2010a). We use 400×400 uniform grids in the $r - \phi$ plane and 40 uniform grids in the

θ direction between $70^\circ - 90^\circ$ with a mirror symmetry in the equatorial plane. This grid can recover all the dust mass from 2D hydrodynamics within a 5% uncertainty. A larger grid number does not change the results. We then run RADMC-3D simulations to compute the dust temperature $T_d(r, \phi, \theta)$ contributed by the stellar radiation. With the dust temperature T_d obtained from RADMC-3D and the dust surface density Σ_d for dust species derived from hydrodynamical simulations, we can calculate the dust continuum by ray-tracing with RADMC-3D.

Table 1. Model parameters and circularization time

model	Σ_0 (g cm^{-2})	α_{vis}	e_p	a_p (au)	s_d (mm)	t_{circ} (orbits) [†]
fiducial	1.4	2×10^{-4}	0.8	100	0.2	2500
HigVis	1.4	1×10^{-3}	0.8	100	0.2	2500
LowMg	0.36	2×10^{-4}	0.5	40	0.2	1600
S2	1.4	2×10^{-4}	0.8	100	0.05	2500
S3	1.4	2×10^{-4}	0.8	100	0.5	2500

NOTE— e_p and a_p are chosen to keep the same pericenter radius of the planet [$a_p(1 - e_p)$] for different models here. [†] Circularization time measured in unit of orbits at $r_0 = 50$ au.

3. RESULTS

3.1. Planet dynamics

We first consider one planet with an initial eccentricity of $e_p = 0.8$ as our fiducial run.

The time evolution of the planet’s stellocentric radius (black) is shown in the upper panel of Figure 1. The specific angular momentum of the planet with an eccentric orbit is defined as $J_p = \sqrt{GM_* a_p (1 - e_p^2)}$. The pericenter and apocenter of the orbit are linked to the planetary angular momentum J_p as $a_{\text{min}} = J_p^2 / [GM_*(1 + e_p)]$ and $a_{\text{max}} = J_p^2 / [GM_*(1 - e_p)]$, respectively. We also plot the eccentricity e_p evolution in the middle panel of Figure 1, which shows that it is damped over ~ 2500 orbits. The increase of the pericenter $a_{\text{min}} = a_p(1 - e_p)$ and the decrease of the apocenter $a_{\text{max}} = a_p(1 + e_p)$ are consistent with the damping of the eccentricity with $e_p = (a_{\text{max}} - a_{\text{min}}) / (a_{\text{max}} + a_{\text{min}})$.

We also show the expected $a_{\text{min},l}$ and $a_{\text{max},l}$ (red) in the upper panel of Figure 1 if the planet’s orbital angular momentum was conserved during the whole evolution. The time derivative of the planet angular momentum is

$$\frac{\dot{J}_p}{J_p} = \frac{1}{2} \frac{\dot{a}_p}{a_p} - \frac{e_p^2}{1 - e_p^2} \frac{\dot{e}_p}{e_p}. \quad (4)$$

As the planet typically migrates inward with $\dot{a}_p < 0$ even for a high e_p , whether the planet gains or loses orbital angu-

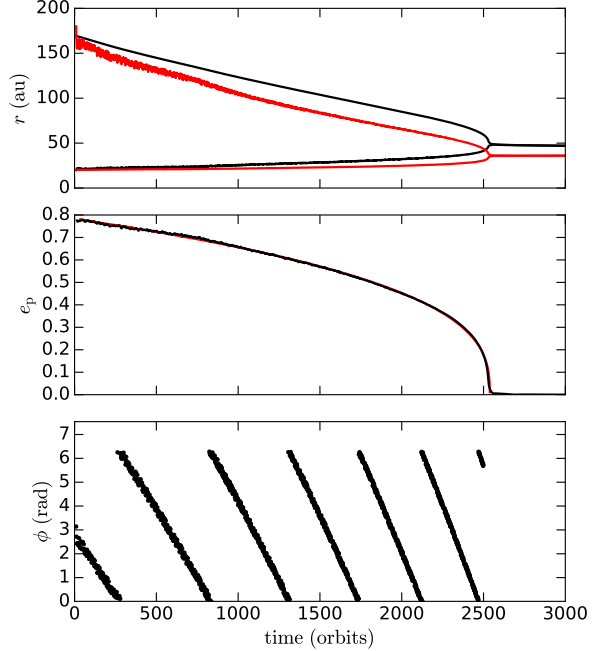


Figure 1. Planet orbit circularization for the fiducial model. Upper panel: black dots show both the planet’s pericenter and apocenter locations from the star as a function of time. Red dots show the expected a_{min} and a_{max} if the angular momentum of the planet was conserved. A larger a_{min} and a_{max} compared with the red dots indicate the transfer of angular momentum from the disk to the planet. Middle panel: the evolution of planet’s orbital eccentricity as a function of orbital period (black line). The red line shows the fit with $de_p/dt = -Ae_p^{-\alpha}$, where the best-fitted $\alpha = 1.83$. Lower panel: the pericenter phase of the planet orbit as a function of time. The periodical variation of the pericenter’s phase suggests a precession period of ~ 450 orbits.

lar momentum depends on the value of e_p . For large initial e_p , the planet gains orbital angular momentum while loses eccentricity. This is consistent with the analytic works (Papaloizou & Larwood 2000; Ida et al. 2019) and N-body simulations (Cresswell, & Nelson 2008) in the supersonic case (i.e., $e_p \gg h_0$).

The gain of planet’s orbital angular momentum yields a circularization radius R_{circ} of the planet at ~ 50 au, which is a factor of ~ 1.4 larger than the value (36 au) if the planet’s angular momentum was conserved. This circularization location is also much farther away from the initial pericenter location (20 au). This presents an interesting case while an initially eccentric planet could eventually be located at a relatively large stellocentric radius on a circular orbit.

We fit the eccentricity evolution with a power-law form of $de_p/dt = -Ae_p^{-\alpha}$, which leads to a timescale $t_{\text{circ}} \equiv$

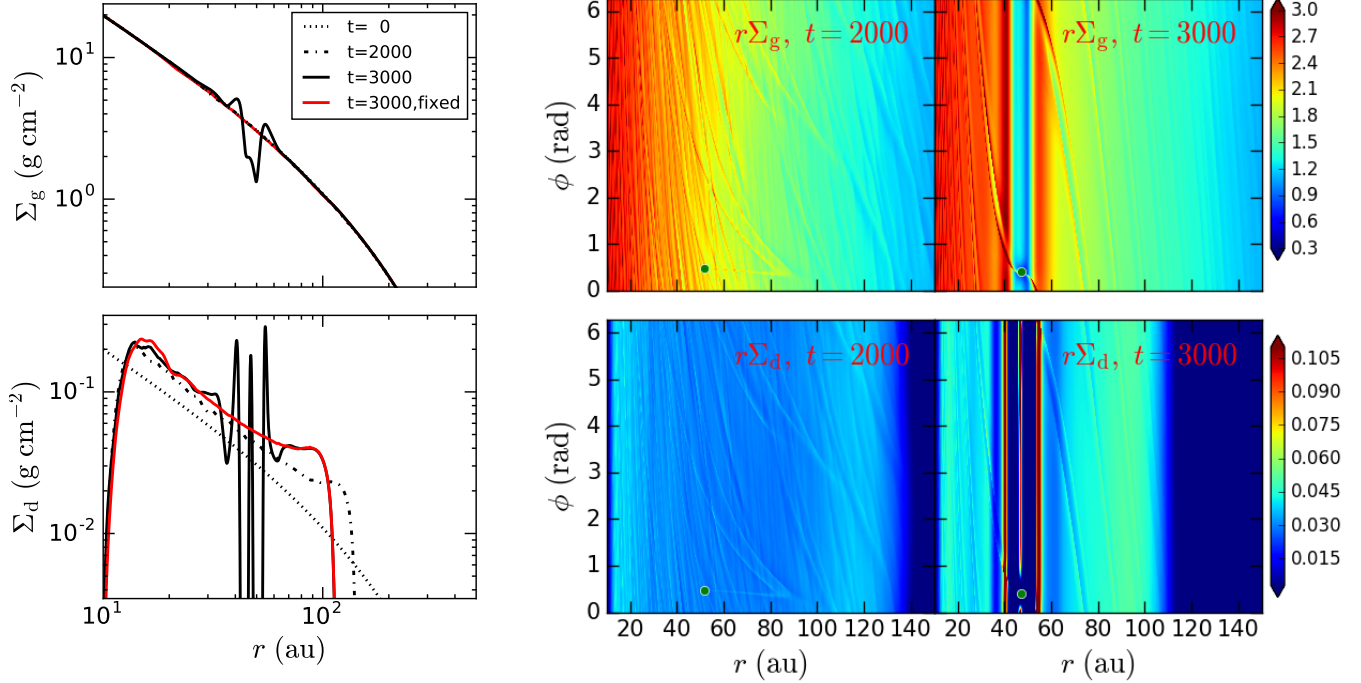


Figure 2. Left panels: Azimuthally-averaged gas (upper) and dust (lower) radial profiles for the fiducial model at different times. The red lines show the radial profiles of gas and dust at 3000 orbits when the planet is fixed to the initial eccentric orbit. Middle panels: 2D gas and dust surface density (multiplied by the radius) for the same model at 2000 orbits (before planet circularization). The planet is shown as the green filled circle. The upper (lower) panel corresponds to gas (dust). Right panels: Same as the middle panels but for 3000 orbits (after planet circularization). Orbital time are all measured at $r_0 = 50$ au, so 3000 orbits correspond to ~ 1.1 Myr.

$\int \frac{de_p}{de_p/dt} = e_{p,0}^{\alpha+1} / A(\alpha+1)^2$. The fitting result is shown as the red line in the middle panel with $\alpha = 1.83$ and the corresponding circularization timescale $t_{\text{circ}} \simeq 2500$ orbits at 50 au, i.e., 0.9 Myr, consistent with the circularization timescale of 0.7–1.1 Myr derived from previous studies (Papaloizou & Larwood 2000; Cresswell, & Nelson 2008; Muto et al. 2011; Ida et al. 2019), using our model parameters.

Our simulation also suggests a scaling relation of $t_{\text{circ}} \propto e_p^{2.8}$, consistent with the previous results of $t_{\text{circ}} \propto e_p^{3.0}$ in high e_p regime (Papaloizou & Larwood 2000; Cresswell, & Nelson 2008; Ida et al. 2019). Meanwhile, the pericenter of the orbit precesses with a period of 450 orbits, as shown in the lower panel of Figure 1.

3.2. Gas and dust evolution

An eccentric planet during and after circularization could leave imprint on the gas and dust distributions. The azimuthal-averaged gas and dust surface density radial profiles are shown in Figure 2. We select three different times to show the temporal evolution of the dust and gas distributions. Initially, both the gas and dust follow the distribution as in

Equation (1). At 0.7 Myr (2000 orbits), which corresponds to the time before the planet is circularized, the gas is only marginally disturbed in the whole disk. The dust also has a relatively smooth distribution except for the truncation at 150 au and a steep drop in the inner boundary. Such a truncation at the outer edge, which shrinks with time gradually, is due to the dust radial drift, while the decrease of the dust in the inner edge is due to the open boundary we choose. This smooth gas/dust distribution is because of the weak dynamical friction force induced for a higher eccentric planet (Muto et al. 2011). The pericenter precession of the planet mentioned above makes its interaction with disk even weaker, which is attributed to a longer time for the planet to encounter the same region of the disk, leading to the recovering of the gas from the disturbance with the viscous timescale.

After the planet is circularized around 2500 orbits, the disk is strongly perturbed around the planet orbit, similar to the situation with a planet on a circular orbit. Two rings sandwiching the gap induced by the planet gradually appear in the gas radial profiles. Accordingly, the dust can be trapped in the two gas bump regions due to the positive pressure gradient near the edges of the gas gap. The density contrast of the gap and rings becomes gradually higher with time because of the continuous dust trapping in the rings, shown as

² This definition of circularization timescale is different from those in previous works by a factor of $1/(\alpha+1)$ (e.g., Papaloizou & Larwood 2000).

the solid line in the left panel of Figure 2, which corresponds to the time at 3000 orbits (i.e., 1.1 Myr). A higher dust-to-gas ratio, ~ 0.1 , is reached for the dust ring.

The 2D distributions for the gas and dust at two evolution stages (2000 and 3000 orbits) are shown in the middle and right panels of Figure 2. We multiply the gas and dust surface density by the radial distance r for illustration purpose. Before the planet circularization (2000 orbits), both the gas and dust are marginally disturbed as shown in middle panels of Figure 2, although some weak spiral features exist around the planet. At 3000 orbits when the planet is in a circular orbit, a prominent gap at the circularization radius is shown in the gas distribution. A deep gap sandwiched by two bright rings then shows up at the same location for the dust distribution. The third dust ring also exists at the planetary co-orbital radius. The three rings are located at ~ 55 au, ~ 47 au and ~ 41 au. The two rings separated by the planet are close to a pair of 3:2 resonance.

For the purpose to compare with ALMA observations, we use RADMC-3D package to produce the 1.33 mm dust continuum, and convolve them with a gaussian beam of $0.03'' \times 0.03''$. The disk is assumed to be at a distance of 140 pc. This beam size is close to the recent highest resolution by ALMA (Andrews et al. 2018). Similar to the discussion above, two snapshot at 2000 and 3000 orbits are chosen to produce the dust image as shown in Figure 3. The featureless image at 2000 orbits is consistent with the smooth dust density distribution. After the planet orbit circularization, remarkable ringed-structures in the dust density distribution (a gap plus several rings around the planet circularization radius) can be recovered. The dust ring location, which is close to the circularization radius, can be in the outer region of the disk because of the angular momentum gaining during the circularization process. This can thus provide a natural explanation for the rings observed at large radii.

We have also tried the case where the planet is kept on a fixed eccentric orbit (i.e., no planet circularization and precession). We find that the gas and dust surface density distributions do not show any visible features and no gaps/rings are produced, shown as the red lines in the left panels of Figure 2. The features shown in Figures 2 and 3 can only be produced after the planet circularization.

3.3. Other models

As we have shown that the dust and gas dynamics are strongly influenced by the planet circularization process, we explore how the final dust distribution depends on the planet, disk, and dust parameters, e.g., disk viscosity α_{vis} , and disk gas surface density Σ_0 , and dust size s_d . Models with different parameters are listed in Table 1. For the purpose of completeness, we have also explored the dependence of the

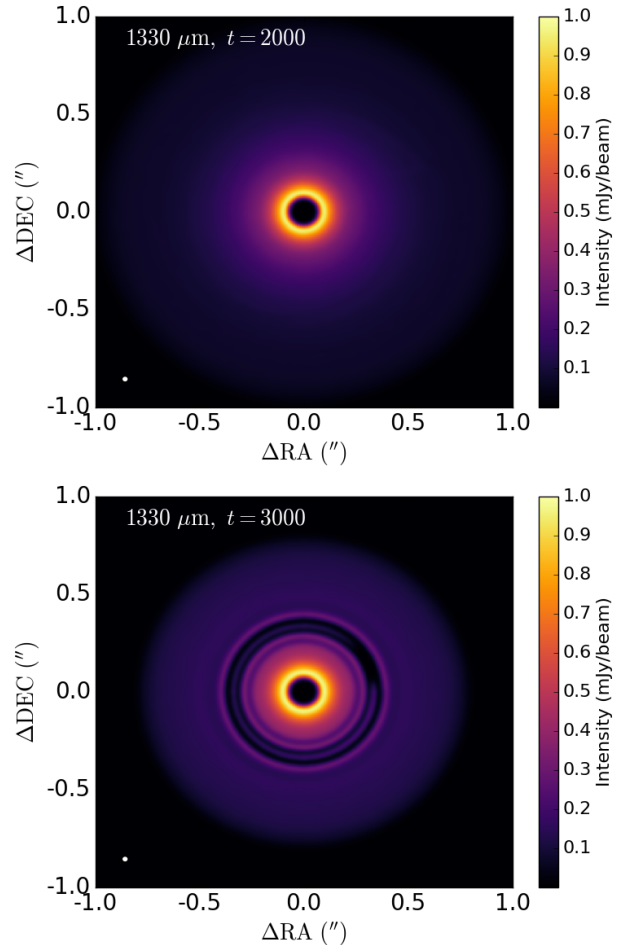


Figure 3. Dust continuum image at $1330 \mu\text{m}$ for two different evolution stages. The upper one is prior to the planet circularization (2000 orbits), while the bottom one is after the circularization (3000 orbits). The planet can only have a significant impact on the dust distribution (i.e., gap/rings) after its circularization.

circularization timescale on the disk scale height in high e_p and low e_p regimes in Appendix B.

3.3.1. Disk mass

We first discuss the effect of disk mass. As the planet circularization timescale is inversely proportional to the disk mass (e.g., Papaloizou & Larwood 2000; Cresswell et al. 2007, also confirmed by our simulations with a different disk mass but with a fixed eccentricity, which is not shown here), we adopt a lower initial eccentricity to allow the faster planet circularization when the disk mass is lower, labeled as model LowMg in Table 1.

We show the circularization process in the left panels of Figure 4. The red lines in the upper left panel is the expected pericenter and apocenter radii if the angular momentum of the planet is conserved. We can see that the angular momentum gaining is not so prominent as in our fiducial

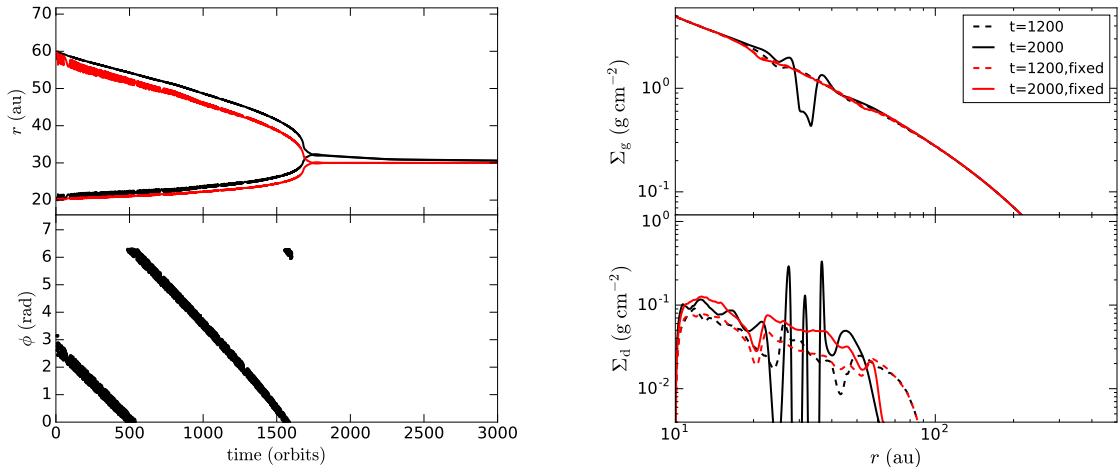


Figure 4. Model with a low gas surface density (LowMg). Upper left panel: planet’s pericenter and apocenter as a function of time. Red curves show the expected pericenter and apocenter if the angular momentum of the planet was conserved. Lower left: the pericenter phase of the planet orbit as a function of time, which suggests a precession period of ~ 1000 orbits. Right panels: azimuthally-averaged gas (upper) and dust (lower) radial profiles at the stage of before circularization (1200 orbits) and after circularization (2000 orbits). For a comparison, we also show the corresponding radial profiles when the planet is fixed at the initial orbit as red lines.

model, which can be understood from Equation (4) in the case of a low initial eccentricity. The circularization radius is thus very close to $\sim a_p(1 - e_p^2) = 30$ au. The precession timescale shown in the lower left panel of Figure 4 becomes much longer compared with our fiducial model, which is related to the low disk mass³. The planet-disk interaction induced planetary precession has been studied for different disk models (Fontana & Marzari 2016; Davydenkova, & Rafikov 2018; Sefilian, & Touma 2019). More detailed comparison with these models will be carried out in future studies.

In the LowMg case, the dust disk becomes significantly smaller because of the larger Stokes number of the dust as defined in Equation (3), which leads to a fast radial drift for the dust. Due to the reduction of the radial drift timescale and the increase of the circularization timescale with decreasing disk gas mass, we would expect that the dust radially drift inside the planet circularization radius when we decrease the disk mass further. In this case, a very compact disk without any ringed-structures would be expected.

The gas sub-structure in the LowMg case can lead to a more prominent dust gap/ring as shown in Figure 4 due to the rapid accumulation of the dust with the fast radial drift. Three rings can be seen around ~ 27 , ~ 31 , and ~ 36 au, respectively, as shown in Figure 4. The rings at 27 au and 36 au are also close to the 3:2 resonance pair.

More interestingly, in the LowMg case, the dust rings/gaps can form *before* the planet circularization as shown in the

right panels of Figure 4, different from other models we studied here. We show the dust emission image at 1200 orbits in the upper panel of Figure 5. There is an outer gap located at 43 au and an inner one located at 25 au, close to the current apocenter and pericenter of the orbit, respectively. We find that such a gap opening process before orbit’s circularization are mainly related to the less massive disk and low disk viscosity. This is due to the density wave damping in the low viscosity disk. The dependence of the density wave launched by the planet on the Toorme Q parameter results in a much more efficient gap opening process when the Q parameter of the disk increases for a lower disk mass (Rafikov 2002; Li et al. 2009). A lower disk viscosity is also essential in making a longer refilling timescale for the gas and producing deeper dust rings as we will show later. In addition, the tidal force on the disk becomes strongest at the pericenter and apocenter locations (Muto et al. 2011). All of these eventually produce the gaps (and rings) at the current apocenter and pericenter locations seen in the top panel of Figure 5. The locations of those gaps/rings evolve with time as the planet circularizes. This gap-opening process does not depend on the planet initial eccentricity too sensitively so long as the initial e_p is high, as tested by our simulations with different initial eccentricities⁴, so long as the viscous timescales are much longer than the gap opening time scale. Since the planet can be circularized at a timescale of $\sim \text{Myr}$, which is comparable to the

³ We find that the precession timescale is quite insensitive to the initial planetary eccentricity, e.g., $e_p = 0.5 \sim 0.8$.

⁴ The models with the same disk mass but with different initial eccentricities ($e_p = 0.5 \sim 0.8$) can produce gaps/rings structures at the pericenter/apocenter locations.

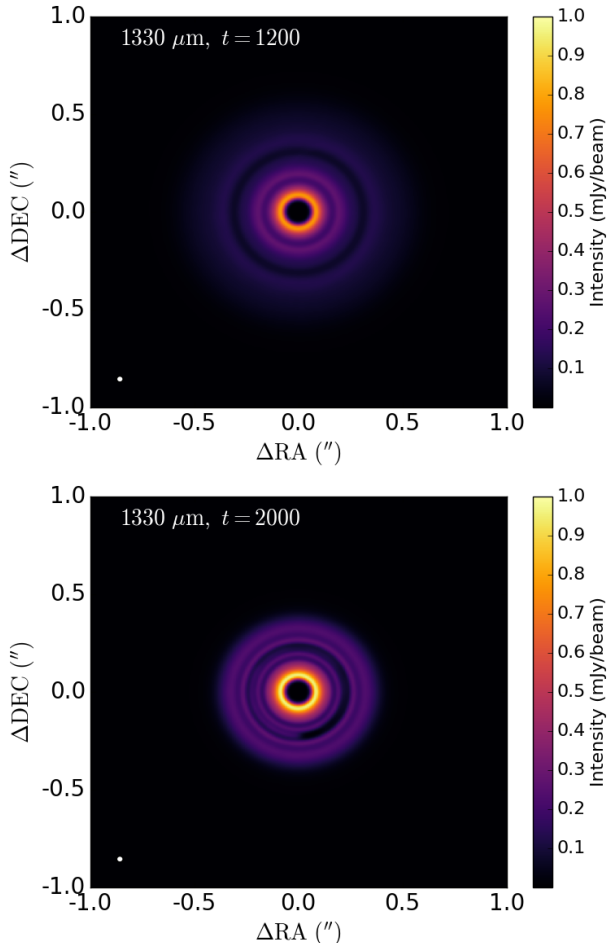


Figure 5. Same as Figure 3 but for model LowMg. The planet is circularized at ~ 1600 orbits, so $t = 1200$ and $t = 2000$ corresponds to the stages before and after the planet circularization. Note that dust rings/gaps are formed both before and after the circularization.

age of most protoplanetary disks, such evolution stage could be caught observationally. The gap opening before the planet circularization cautions against using the gap and ring location to infer the current planetary orbital radius.

To quantify the role of planet dynamics in the gap opening process, we test the case with the planet fixed on its initial eccentric orbit. The radial profiles of gas and dust are shown in the right panels of Figure 4. Compared with the profiles at 1200 orbits in the LowMg model, the gap/rings are also present around the pericenter, although the features at the apocenter become weaker. This again indicates that the gap opening process is mainly controlled by the low disk mass (equivalently, a larger Toomre Q parameter) and the low viscosity (Rafikov 2002; Li et al. 2009). An eccentric orbit produces an inefficient gap opening process due to the weak dynamical friction force in the high e_p regime (Muto et al. 2011).

As these processes all depend on how the angular momentum flux is transported throughout the disk, the effect due to an adiabatic EoS versus locally isothermal condition is investigated. Miranda & Rafikov (2019) recently found that the locally isothermal EoS is inaccurate to capture rings/gaps features under certain conditions, including when the the disk is nearly inviscid and the planet mass is small (less than thermal mass). Here, we find out that the inaccurate treatment from the locally isothermal EoS does not produce any significant differences on our main results. The details are described in Appendix A.

3.3.2. Disk viscosity

We then consider the model HigVis with a higher α_{vis} . The planet dynamics (circularization radius, timescale) is almost the same as our fiducial model as shown in Figure 6. After the planet’s circularization, the migration rate significantly increases, different from the very slow migration with the smaller viscosity as shown in Figure 1. This is also consistent with previous works by Li et al. (2009) and Yu et al. (2010). The fast inward migration of the planet causes the gaps/rings move closer to the central region after a longer evolution time. A smaller gap depth is also attributed to the high viscosity (Fung et al. 2014; Kanagawa et al. 2015; Zhu 2019). A shallower gap of the gas distribution for the high viscosity model leads to the dust gap and ring being shallow as well, which further makes the detection of such gap/rings harder.

3.3.3. Dust sizes

We find that the incorporation of dust has almost no impact on planet dynamics, while the dust size is a factor that can influence the dust radial drift. We can, therefore, explore the dust ring formation by adopting different dust sizes. We compare the dust distributions for $s_d = 0.05$ mm and $s_d = 0.5$ mm with our fiducial model in Figure 7, where dust can only be significantly perturbed after the planet circularization.

We find that the overall size of the dust disk gradually gets smaller when the dust size increases from $s_d = 0.05$ mm (red) to $s_d = 0.5$ mm (green), although the gas distribution remains the same. For all models, the dust gap/rings appear in the same location due to the same planet circularized radius, though the dust concentration in rings as compared to the surrounding regions can vary. They all have three rings similar with our fiducial model with $s_d = 0.2$ mm.

In particular, for Model S3 with $s_d = 0.5$ mm, the dust drifts radially quicker than our fiducial model but the dust radial drift is almost halted at the planet’s circularization radius. As shown in the lower panel of Figure 7, the outer dust ring at 1.4 Myr is almost the same as that at 1.1 Myr. In contrast, such dust would have drifted significantly inward between 1.1 and 1.4 Myr if there is no planet (shown as the

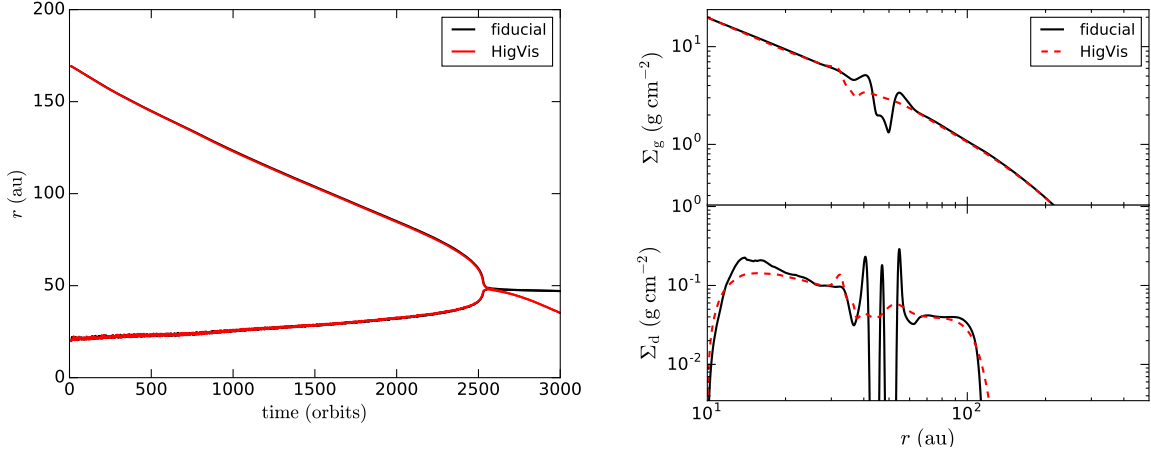


Figure 6. Models with different disk viscosities. Left: planet’s pericenter and apocenter as a function of time. The model with a high viscosity (HigVis) shows a similar circularization process with our fiducial model. Right: Azimuthally-averaged gas (upper) and dust (lower) radial profiles. All radial distributions are shown at 3000 orbits when the planet is circularized.

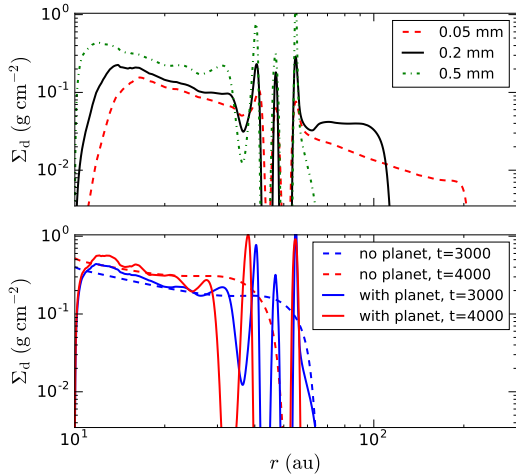


Figure 7. The effect of dust sizes on the ring formation. Upper: Azimuthally-averaged dust radial profiles at $t = 3000$ orbits with different dust sizes based on Model S2 (red), fiducial (black) and S3 (green), respectively. Lower: Effect of a planet on the radial drift of the large-sized dust. The planet case corresponds to model S3.

dash lines in the bottom panel of Figure 7). This suggests that, depending on the interplay among several timescales for the dust drift, planet orbital circularization, and gap opening processes, the circularized planet orbit can effectively stop the dust drift at large disk radii, accompanied with relatively narrow, dense dust rings.

4. CONCLUSIONS

In this work, we have performed 2D high-resolution hydrodynamical simulations with LA-COMPASS (Li et al. 2005, 2009; Fu et al. 2014) to study the interaction of a highly eccentric super-Earth with a dusty gaseous disk. The highly ec-

centric super-Earth initialized in our simulations is the main assumption in this work, which is motivated by the scenario that many planets can form at small radii but some can be scattered into highly eccentric orbits. One single dust species is implemented in gas-dust disk dynamics with self-consistent feedback. Disk self-gravity is also included. With the long time evolution of the coupled gas/dust and the embedded planet, we study the planet circularization process, its consequent impact on the dust dynamics, and the observational features as well. We also explore how different disk mass, viscosity, planetary parameters and dust size can influence the appearance of dust rings.

We confirm the parameter dependence of circularization timescale on the initial eccentricity, disk mass, and disk scale height in previous works (Papaloizou & Larwood 2000; Cresswell, & Nelson 2008; Muto et al. 2011; Ida et al. 2019). A higher viscosity can speed up the migration rate significantly after the planet’s circularization, but has no influence on the planetary dynamics before its circularization. The inclusion of dust has almost no impact on the planetary circularization and migration processes. Our main findings are summarized as follows, mostly applicable to situations with initially high orbital eccentricity:

- The planet’s orbit gains angular momentum when the initial planetary eccentricity is high enough, consistent with the results using analytic analysis and N-body simulations. This results in a large circularization orbital radius for the planet. The planet opens up a partial gap in gas, producing dust gaps and rings around the circularization radius after planet’s circularization. This could explain the gaps/rings observed at the outer region of disks. Before the circularization or when we fix the planet at its initial eccentric orbit, the distur-

bance of the planet on the dusty disk is very weak when the disk mass is high ($\sim 0.02 M_\odot$).

- When the disk mass is low ($\sim 5 \times 10^{-3} M_\odot$), however, we find that gaps and rings can be produced at the current pericenter and apocenter location even before its orbital circularization for a low disk viscosity. This is also true when we fix the planet at the initial eccentric orbit. This cautions against using the gap and ring location to infer the current planetary orbital radius.
- An eccentric planet can potentially slow down the dust radial drift in the outer region of the disk, particularly when the planet's orbit is circularized faster than the radial drift timescale and a low disk viscosity that slows down the planetary inward migration. The dust drift is stopped at the rings with relatively little emission from the surrounding regions. Observations at longer wavelengths tracing the large dust particles will be particularly useful in constraining this configuration.

We have explored a relatively straightforward limit with a single super-Earth planet on an eccentric orbit. Configurations with multiple planets (perhaps with a mixture of massive and smaller planets) will also be quite interesting. As some of the observed protoplanetary disks are relatively old with possibly low total disk mass, the circularization timescales for such planets can be long, exceeding 1 Myr. It is then imperative to include these processes when interpreting the origin and mechanisms for dust ring and gap formation.

We thank the referee for very helpful comments to improve the presentation of the paper. YPL, HL and SL gratefully acknowledge the support by LANL/CSSES and NASA/ATP. Simulations of this work were performed with LANL Institutional Computing resources. HL gratefully acknowledges useful discussions with S. Ida, R. Miranda and R. Rafikov.

Software: Astropy (Astropy Collaboration et al. 2013), LA-COMPASS (Li et al. 2005, 2009), Matplotlib (Hunter 2007), Numpy (van der Walt et al. 2011), RADMC-3D (Dullemond et al. 2012)

APPENDIX

A. THE EFFECT OF ADIABATIC DISKS

Recently, Miranda & Rafikov (2019) found that the locally isothermal simulations tend to overestimate the contrast of rings/gaps, and even mis-identify the planet position that is responsible those features. To quantify this effect on our simulation results, we choose the run LowMg to compare with another run where we incorporate the energy equation with an adiabatic index $\gamma = 1.001$ as in Miranda & Rafikov (2019), while keeping all other parameters being the same. We do not implement dust in the adiabatic run as in Miranda & Rafikov (2019), since we found that dust has no impact in the planet dynamics and the feedback effect on the gas is small.

In Figure 8, we show the radial profile of the integrated angular momentum flux (AMF) at 2000 orbits (left), and the planet circularization process (middle), and the radial distribution of gas surface density (right) at two different times (corresponding to 1200 and 2000 orbits) for our locally isothermal case and the adiabatic one. The discrepancy of AMF is only marginal for the region where the planet is circularized (~ 30 au). The offset beyond $r = 60$ au could be the imprint of the planetary circularization process, which, however, does not leave significant features on the gas. This is actually consistent with the expectation from Miranda & Rafikov (2019). When the planet mass is $M_p = 1 M_{\text{th}}$, where the thermal mass $M_{\text{th}} = h_{0,p}^3 M_\star \simeq 7 M_\oplus$ (here we measure the disk scale height at the initial semi-major axis a_p), the error caused by the locally isothermal case is not significant. Furthermore, we find that the circularization timescale and the circularization radius are almost the same for these two case, as shown in the middle panel of Figure 8. Such an indistinguishable planet dynamics leads to the similar gas surface density profile as shown in the right panel of Figure 8. Therefore, we should also expect that the impact on the dust distribution in terms of the dust ring appearance and their locations should be insignificant if we use a similar adiabatic EoS.

B. PARAMETER DEPENDENCE OF PLANET CIRCULARIZATION TIMESCALE

Here we further explore the non-linear dependence of the planet circularization timescale on the disk scale height (or sound speed).

Since the inclusion of dust does not change the dynamics of the planet, we only consider a pure gaseous disk without dust. Our default disk gas mass is $2 \times 10^{-2} M_\odot$ with the same radial distribution as in Equation (1). The other default parameters are $M_p = 10 M_\oplus$, and a softening factor of $0.7h_g$ as our fiducial model. The planetary semi-major axis is $r_p = 2.0$ in code unit with $r_0 = 50$ au. We explore two regimes, one is $e_p \gg c_{s,0}$ (i.e., the supersonic case), where $c_{s,0}$ is the sound speed at the initial planetary semi-major axis ($c_{s,0} = r_p^{0.25} h_0$), and the other one is $e_p \lesssim c_{s,0}$ (i.e., the subsonic case). For the supersonic case, we fit the time evolution profile of the eccentricity as shown in the middle panel of Figure 1 with $de_p/dt = -Ae_p^{-m}$. The

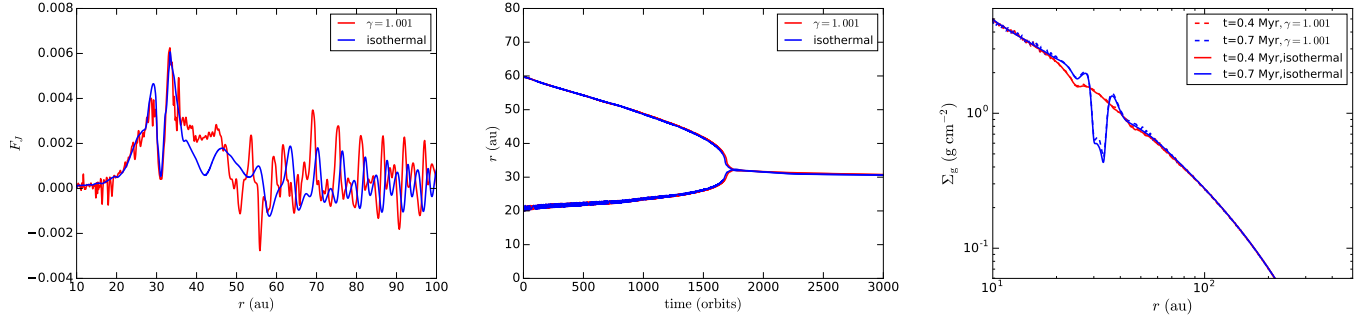


Figure 8. The effect of adiabatic EoS ($\gamma = 1.001$) vs. the locally isothermal LowMg run on the planet dynamics and gas surface density profiles. Left: radial profiles of the planet-induced angular momentum flux in the code unit at 2000 orbits. Middle: the planetary orbital apocenter and pericenter as a function of time. The isothermal and adiabatic with $\gamma = 1.001$ runs are almost indistinguishable. Right: the radial distributions of the gas surface density at two times ($t = 1200$ and 2000 orbits) for two runs. Again, the difference is small.

circularization timescale is then $t_{\text{circ}} = e_p^{\alpha+1}/A(\alpha + 1)$. For the subsonic case, it has been suggested that t_{circ} is independent of the initial eccentricity e_p (Papaloizou & Larwood 2000), so we fit the temporal eccentricity profile for the very low eccentricity part ($e_p \ll h_0$) with $de_p/dt = -Ae_p$. And we define the corresponding circularization timescale $t_{\text{circ}} = 1/A$. We have six runs with three different h_0 as shown in Figure 9 for two regimes.

We use a single power-law model $t_{\text{circ}}(h_0) \propto h_0^{-m}$ to quantify the dependence of t_{circ} on h_0 . We find that the power-law index is $\alpha \sim 1.3$ for the low eccentricity regime (subsonic case), while $\alpha \sim 4.0$ for the high eccentricity regime (supersonic case), close to the expectation of the functional form from Papaloizou & Larwood (2000) and Ida et al. (2019). The slight difference of m in the high eccentricity regime could be due to the softening effect and the transition average between supersonic and subsonic regimes.

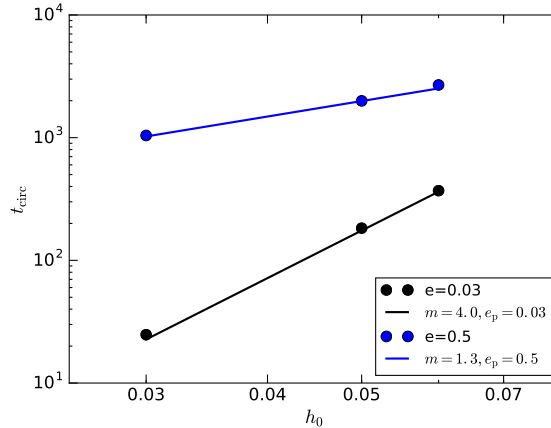


Figure 9. Parameter dependence of circularization timescale (t_{circ}) on the disk scale height h_0 at r_0 (or the sound speed). We use a simple power-law model to quantify the dependence of t_{circ} on h_0 in the high e_p and low e_p regimes.

REFERENCES

- ALMA Partnership, Brogan, C. L., Pérez, L. M., et al. 2015, *ApJL*, 808, L3
 Andrews, S. M., Huang, J., Pérez, L. M., et al. 2018, *ApJ*, 869, L41.
 Andrews, S. M., Wilner, D. J., Zhu, Z., et al. 2016, *ApJL*, 820, L40
 Ansdell, M., Williams, J. P., Trapman, L., et al. 2018, *ApJ*, 859, 21
 Arzamasskiy, L., Zhu, Z., & Stone, J. M. 2018, *MNRAS*, 475, 3201
 Astropy Collaboration, Robitaille, T. P., Tollerud, E. J., et al. 2013, *A&A*, 558, A33

- Birnstiel, T., Dullemond, C. P., & Brauer, F. 2010a, *A&A*, 513, A79
- Bitsch, B., Crida, A., Libert, A.-S., & Lega, E. 2013, *A&A*, 555, A124
- Boehler, Y., Ricci, L., Weaver, E., et al. 2018, *ApJ*, 853, 162
- Cieza, L. A., Casassus, S., Pérez, S., et al. 2017, *ApJL*, 851, L23
- Clarke, C. J., Tazzari, M., Juhasz, A., et al. 2018, *ApJ*, 866, L6.
- Cox, E. G., Harris, R. J., Looney, L. W., et al. 2017, *ApJ*, 851, 83
- Cresswell, P., Dirksen, G., Kley, W., & Nelson, R. P. 2007, *A&A*, 473, 329
- Cresswell, P., & Nelson, R. P. 2008, *A&A*, 482, 677
- D'Angelo, G., Lubow, S. H., & Bate, M. R. 2006, *ApJ*, 652, 1698.
- Davydenkova, I., & Rafikov, R. R. 2018, *ApJ*, 864, 74
- Dipierro, G., Ricci, L., Pérez, L., et al. 2018, *MNRAS*, 475, 5296
- Dipierro, G., Price, D., Laibe, G., et al. 2015, *MNRAS*, 453, L73
- Dong, R., Li, S., Chiang, E., et al. 2017, *ApJ*, 843, 127
- Dong, R., Li, S., Chiang, E., et al. 2018b, *ApJ*, 866, 110
- Dong, R., Liu, S.-yuan., Eisner, J., et al. 2018a, *ApJ*, 860, 124
- Dong, R., Zhu, Z., & Whitney, B. 2015, *ApJ*, 809, 93.
- Duffell, P. C., & Chiang, E. 2015, *ApJ*, 812, 94
- Dullemond, C. P., Juhasz, A., Pohl, A., et al. 2012, *Astrophysics Source Code Library*, ascl:1202.015
- Fedele, D., Tazzari, M., Booth, R., et al. 2018, *A&A*, 610, A24
- Fontana, A., & Marzari, F. 2016, *A&A*, 589, A133
- Fu, W., Li, H., Lubow, S., Li, S., & Liang, E. 2014, *ApJL*, 795, L39
- Fung, J., Shi, J.-M., & Chiang, E. 2014, *ApJ*, 782, 88
- Gonzalez, J.-F., Laibe, G., Maddison, S. T., et al. 2015, *MNRAS*, 454, L36.
- Goldreich, P., & Sari, R. 2003, *ApJ*, 585, 1024
- Goldreich, P., & Tremaine, S. D. 1978, *Icarus*, 34, 240
- Goldreich, P., & Tremaine, S. 1980, *ApJ*, 241, 425
- Hunter, J. D. 2007, *Computing in Science and Engineering*, 9, 90
- Ida, S., et al. 2019, in preparation
- Isella, A., Guidi, G., Testi, L., et al. 2016, *Physical Review Letters*, 117, 251101
- Isella, A., Huang, J., Andrews, S. M., et al. 2018, *ApJL*, 869, L49
- Isella, A., Carpenter, J. M., & Sargent, A. I. 2009, *ApJ*, 701, 260
- Jin, S., Li, S., Isella, A., et al. 2016, *ApJ*, 818, 76
- Jurić, M., & Tremaine, S. 2008, *ApJ*, 686, 603.
- Kanagawa, K. D., Muto, T., Tanaka, H., et al. 2015, *ApJL*, 806, L15
- Kozai, Y. 1962, *AJ*, 67, 591.
- Lega, E., Morbidelli, A., & Nesvorný, D. 2013, *MNRAS*, 431, 3494.
- Li, H., Colgate, S. A., Wendroff, B., & Liska, R. 2001, *ApJ*, 551, 874
- Li, H., Lubow, S. H., Li, S., & Lin, D. N. C. 2009, *ApJL*, 690, L52
- Li, H., Li, S., Koller, J., et al. 2005, *ApJ*, 624, 1003
- Li, S., Buoni, M. J., & Li, H. 2009, *ApJS*, 181, 244
- Li, Y.-P., Li, H., Ricci, L., et al. 2019, *ApJ*, 878, 39
- Lidov, M. L. 1962, *Planet. Space Sci.*, 9, 719.
- Long, F., Pinilla, P., Herczeg, G. J., et al. 2018, *ApJ*, 869, 17
- Loomis, R. A., Öberg, K. I., Andrews, S. M., & MacGregor, M. A. 2017, *ApJ*, 840, 23
- Miranda, R., Li, H., Li, S. et al. 2017, *ApJ*, 835, 118
- Miranda, R., & Rafikov, R. R. 2019, *ApJL*, 878, L9
- Marzari, F., Baruteau, C., & Scholl, H. 2010, *A&A*, 514, L4.
- Moekel, N., & Armitage, P. J. 2012, *MNRAS*, 419, 366.
- Muto, T., Takeuchi, T., & Ida, S. 2011, *ApJ*, 737, 37
- Okuzumi, S., Momose, M., Sirono, S.-i. et al. 2016, *ApJ*, 821, 82.
- Papaloizou, J. C. B., & Larwood, J. D. 2000, *MNRAS*, 315, 823
- Papaloizou, J. C. B., Nelson, R. P., & Masset, F. 2001, *A&A*, 366, 263
- Pinilla, P., Birnstiel, T., Ricci, L., et al. 2012, *A&A*, 538, A114
- Pinilla, P., de Juan Ovelar, M., Ataiee, S., et al. 2015, *A&A*, 573, A9.
- Rafikov, R. R. 2002, *ApJ*, 572, 566
- Rasio, F. A., & Ford, E. B. 1996, *Science*, 274, 954.
- Ricci, L., Testi, L., Natta, A., et al. 2010a, *A&A*, 512, A15
- Rosotti, G. P., Booth, R. A., Clarke, C. J., et al. 2017, *MNRAS*, 464, L114.
- Sefilian, A. A., & Touma, J. R. 2019, *AJ*, 157, 59
- Shakura, N. I., & Sunyaev, R. A. 1973, *A&A*, 24, 337
- Sheehan, P. D., & Eisner, J. A. 2018, *ApJ*, 857, 18
- Suriano, S. S., Li, Z.-Y., Krasnopolsky, R., et al. 2017, *MNRAS*, 468, 3850.
- Suriano, S. S., Li, Z.-Y., Krasnopolsky, R., et al. 2018, *MNRAS*, 477, 1239.
- Takahashi, S. Z., & Inutsuka, S.-ichiro. 2014, *ApJ*, 794, 55.
- Takeda, G., & Rasio, F. A. 2005, *ApJ*, 627, 1001.
- Takeuchi, T., & Lin, D. N. C. 2002, *ApJ*, 581, 1344
- Tanaka, H., Takeuchi, T., & Ward, W. R. 2002, *ApJ*, 565, 1257
- Tanaka, H., & Ward, W. R. 2004, *ApJ*, 602, 388
- Tsukagoshi, T., Nomura, H., Muto, T., et al. 2016, *ApJL*, 829, L35
- van der Marel, N., Dong, R., di Francesco, J., Williams, J. P., & Tobin, J. 2019, *ApJ*, 872, 112
- van der Walt, S., Colbert, S. C., & Varoquaux, G. 2011, *Computing in Science and Engineering*, 13, 22
- van Terwisga, S. E., van Dishoeck, E. F., Ansdell, M., et al. 2018, *A&A*, 616, A88.
- Wu, Y., & Lithwick, Y. 2011, *ApJ*, 735, 109.
- Yu, C., Li, H., Li, S., Lubow, S. H., & Lin, D. N. C. 2010, *ApJ*, 712, 198
- Zhang, K., Blake, G. A., & Bergin, E. A. 2015, *ApJ*, 806, L7
- Zhu, Z. 2019, *MNRAS*, 483, 4221